2024 IEEE International Conference on Robotics and Automation (ICRA 2024)
May 13-17, 2024. Yokohama, Japan

High-speed interfacial flight of an insect-scale robot

Hang Gao[1], Sunghwan Jung[2], E. Farrell Helbling[3]

***Abstract*— Several insect species are able to locomote across the air-water interface by leveraging surface tension to remain above the water surface. A subset of these insects, such as the stonefly and waterlily beetle, flap their wings to actively move around the two dimensional surface — a locomotion strategy referred to as interfacial flight. Here, we present an insect-scale robot, the γ-bot, inspired by these interfacial fliers. The robot is comprised of a flapping-wing vehicle that generates a thrust force parallel to the water surface, and three passive legs utilize surface tension to support the body mass and maintain contact with the air-water interface. We developed and validated a simple model to characterize the drag forces acting on the vehicle and estimate the robot's velocity. This $112\,\mathrm{mg}$ robot can reach maximum velocities of $0.9\,\mathrm{m\,s^{-1}}$ (corresponding to $15\,\mathrm{BL\,s^{-1}}$) and can initiate both left and right turns, demonstrating high maneuverability along the air-water interface. In addition, the robot can carry an additional $419\,\mathrm{mg}$, enabling future sensing, control, and power autonomous operation.**

I. Introduction

The water-air interface provides unique opportunities for mm-scale locomotion. Surface tension, the force per length acting on the contact line between a floating body and the water-air interface, dominates over inertial forces at mm-scales, enabling small objects to stick to the surface. This relationship is described by the Baudoin number [1], $Ba = mg/\gamma P$, where mg is the object's weight and γP is the maximum surface tension force. Insects with $Ba < 1$, like water striders and fishing spiders, can remain at the interface without active locomotion strategies, their legs provide long contact lines with the surface, increasing surface tension relative to their low mass [1]–[4]. Thus, insects can remain at the water interface with very low energy consumption compared to other aerial and aquatic animals that need to constantly flap their appendages to remain at on the surface. In order to move along the interface, these insects generate surface waves, imparting momentum to the water to generate locomotion. Honeybees, when trapped on the water surface, use their wings as hydrofoils, generating asymmetric waves to achieve thrust [5]. Stoneflies and waterlily beetles perform interfacial flight, where the insect's body weight is supported by surface tension, and flapping wings generate propulsion along the water's surface [6]. Water striders use a sculling motion in their middle appendages to generate the power stroke along the water [7].

Using these semi-aquatic insects for inspiration, roboticists have developed a number of high-performance micro-aquatic vehicles (MAVs). Robots have demonstrated rowing [7]–[10], walking [11]–[16], jumping [17], capillary climbing [18], and Marangoni propulsion [19]–[21] to locomote across the air-water interface at up to $2\,\mathrm{BL\,s^{-1}}$(body length per second). Recently, robots have generated propulsion through flapping-wing flight along the water surface [22], [23]. With a single piezoelectric actuator, the $165\,\mathrm{mg}$ robot presented in [22] operated at $280\,\mathrm{V}$ and $105\,\mathrm{Hz}$ to generate forward propulsion at $3\,\mathrm{BL\,s^{-1}}$ and could support loads up to $830\,\mathrm{mg}$. The single actuator limits the operating range of the vehicle because it cannot generate asymmetric forces to turn the vehicle. The RoboFly has also recently demonstrated interfacial flight capabilities. The $100\,\mathrm{mg}$ robot can initiate turns and travel at more than $1.4\,\mathrm{BL\,s^{-1}}$ while flapping at $35\,\mathrm{Hz}$ [23].

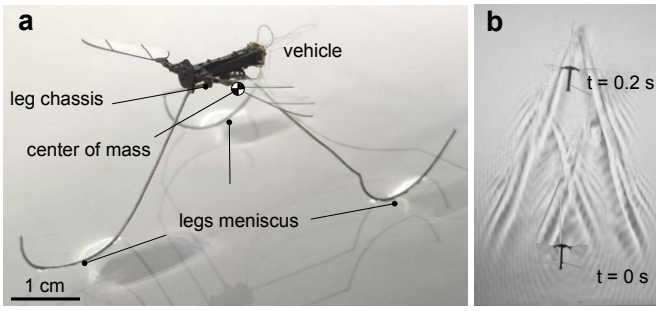

Fig. 1. The $112\,\mathrm{mg}$ γ-bot. A flapping wing robot that can generate propulsion along the air-water interface. a) Perspective view of the robot. The wingspan is 3.6cm, and the overall dimensions of the robot are 5.8cm×3.6cm×2.1cm. b) Interfacial flight demonstration.

Adding to this growing field of interfacial flying robots, our γ-bot (seen in Fig. 1a) generates propulsion through flapping wings and maintains contact with the air-water interface using three supporting legs. Two piezoelectric actuators independently drive each wing, enabling asymmetric force production around the center of mass. The robot is capable of performing straight line locomotion (as seen in Fig. 1b), as well as turning left and right. Our $112\,\mathrm{mg}$ robot achieves speeds up to $0.9\,\mathrm{m\,s^{-1}}$, or $15\,\mathrm{BL\,s^{-1}}$, five times faster than the current state of the art [22]. Because of our ability to generate high speed horizontal locomotion, it is important to characterize the forces that act on the vehicle, including aerodynamic drag on the body, water drag, added mass of the water, and the capillary drag at higher speeds ($>0.23\,\mathrm{m\,s^{-1}}$) [24]. In addition, our leg design supports an additional $419\,\mathrm{mg}$ for future autonomy experiments. The paper is divided into the following sections: Section II details the robot design and manufacturing of the legs, Section III defines the forces acting on the vehicle and presents a simplified model for straight-line locomotion, Section

[1]School of Mechanical & Aerospace Engineering, [2]School of Biological & Environmental Engineering, [3]School of Electrical & Computer Engineering, Cornell University, Ithaca, NY 14580. Contact e-mail farrell@cornell.edu

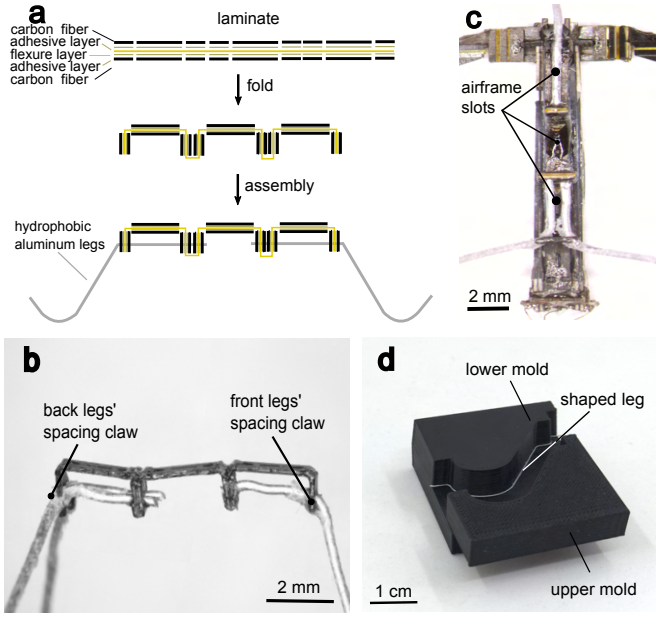

Fig. 2. Overview of the chassis design and leg mold. a) The chassis fabrication process starting from a 2D laminate to a 3D structure that houses the legs. b) assembled chassis with legs, before attachment to the airframe. Total mass is 37 mg. c) Chassis attachment location to the robot airframe (underside of the vehicle). d) 3D printed leg shaping mold.

IV characterizes the robot's performance and validates the model, Section V describes additional robot capabilities for future experiments.

II. Robot Design

Our robot incorporates the flapping-wing vehicle described in [25]. The selection of transmission and wing hinge stiffnesses were experimentally characterized to ensure proper flapping kinematics at resonance (described in Section IV). To support the weight of the vehicle and minimize drag force during horizontal locomotion, we explored various leg designs, described in detail below.

A. Chassis design and manufacturing

The chassis is a simple hinge structure that mates the legs to the airframe of the vehicle. This additional structure enables quick attachment and detachment of the legs, allowing us to iterate through multiple leg designs and ensure consistent attachment. We manufactured the chassis using the smart composite microstructures (SCM) process [26] that creates 3D structures from 2D laminates by folding at flexible joints (see Fig. 2a). To minimize weight, we selected carbon fiber as our structural element (3-ply QA112, 78 µm thickness, Toho Tenax) and polyimide as our flexural layer (100HN Kapton, 25.4 µm). These layers were bonded together using heat-activated adhesive (Pyralux 1500, 12.7 µm, Dupont). We patterned individual layers using a UV laser with 20 µm precision (Protolaser U4, LPKF), pin-aligned and cured under temperature and pressure. After releasing the parts from the laminate, the chassis was folded and fixed using cyanoacrylate glue (Loctite 416). We can then insert the legs into the chassis using pre-patterned guides. The chassis then attaches to the airframe, locking the structure in place with UV glue, see Fig. 2c.

B. Leg design and manufacturing

The legs of the robot play an important role when moving on the interface — they should be relatively light and stiff to support the weight of the vehicle, but easy to form. Previous insect-scale robots that operate on the water surface use a variety of materials for the legs, including Nitinol [17] to store energy and jump from the water surface, carbon fiber to minimize mass in a multimodal vehicle [23], and titanium alloy [22]. Additionally, hydrophobic coatings increase surface tension, and thus enable larger robot payloads. For our robot, we selected aluminum wire (1100 aluminum wire, D =0.33 mm, McMaster-Carr) because it is easy to shape at room temperature.

We designed 3D-printed (i3, PRUSA) molds to bend the aluminum wire to the desired shape, as seen in Fig. 2d. We added an additional 3° to the curve of the leg to compensate for the springback of the aluminum wire when released from the mold [27]. We included FR4 locators to guide the leg into the chassis and distribute force during assembly to prevent the legs from being forced out of the desired shape. Finally, we coated the legs in a superhydrophobic material (Ultra-Ever Dry, UltraTech International Inc.) to increase the contact angle with the water surface [22], [23].

To match similar semi-aquatic insects, we want $Ba \approx 0.2$ [6]. With a vehicle mass of approximately 110 mg, the maximum wetted length, P, needs to be 57 mm. The shape of the curve is a function of the total length and the height of the meniscus. We selected a height of approximately 4.5 mm, to ensure that we achieve maximum surface tension force before the meniscus breaks. In addition, rounded legs have a linear relationship between surface tension force and height of the meniscus, simplifying control in future work [17]. Finally, we needed to ensure that distal tip of the leg extended above the surface of the water to not break the meniscus when driving the robot at high speeds. The final design incorporated three legs, one in front of the vehicle and two behind, stabilizing the vehicle during high speed skating maneuvers and minimizing water drag and steering friction to increase velocity and execute turns. The final robot can be seen in Fig. 1.

III. Modeling and Vehicle Dynamics

During interfacial flight, reaction forces on the body include horizontal air drag ($F_{D,body}$), horizontal capillary drag (F_c), vertical and horizontal water drag ($F_{D,leg}$), as well as vertical and horizontal surface tension ($F_{s,X}$,$F_{s,Y}$) [28]. Because the γ-bot's body angle is parallel with the water surface, it generates thrust primarily in the horizontal x-direction (see Fig. 3 for a depiction of the planar dynamic model). Neglecting asymmetric forces on the wings and assuming minimal angular velocities in forward locomotion, we can reduce the linear momentum balance equation to the sum of the forces in the x-direction:

$$m\ddot{X} \simeq F_{thrust} - F_{D,leg} - F_c - F_{s,X} - F_{D,body}. \quad (1)$$

In the vertical direction, the mass of the robot (m_r) is balanced by the surface tension force, $m_r g = F_s, Y(h)$. We neglect contributions from buoyant force, as $Ba < 1$. In the following subsections, we detail our equations and assumptions for each component of these force equations.

A. Surface Tension

In the vertical direction, we can model the aluminum legs as cylinders floating on a liquid-gas interface. As demonstrated in [17], [29], the surface tension force of the leg equation becomes:

$$\frac{F_{s,Y}(h)}{N} = \int f_{s,Y}(h) dL_s \approx \int 2\rho_w g l_c h \sqrt{1-(h/2l_c)^2} dL_s, \tag{2}$$

where $f_s(h)$ is the vertical surface tension force per unit of wetted length, ρ_w is water density, g is the gravitational acceleration, $l_c = \sqrt{\gamma/(\rho_w g)}$ is the capillary length of water [30], and h is the immersed depth of the meniscus. As can be seen in this equation, the surface tension is both a function of the wetted length of the legs L_s, and the height, h of the dimple. While an increase in the wetted length increases the magnitude of the surface tension force, and thus the total payload that the robot can carry, it also increases the amount of drag force acting on the vehicle as it is moving along the water's surface, as described later in this section.

During locomotion, the contact angles at the front and rear of the legs (α_1 and α_2) will vary, and the meniscus at the rear part of the leg extends from ψ_1 to ψ_2, as shown in the inset of Fig. 3. We assume that the contact angle varies linearly from the front to the rear part of the leg and employ the method of infinitesimals to compute the difference in surface tension.

$$\frac{F_{s,X}(\psi)}{N} = \int f_{s,X} dL_s = \int_{\psi_1}^{\psi_2} 2\gamma \cos\alpha(\psi) dR_L \sin\psi, \tag{3}$$

where $\cos\alpha(\psi)$ =slope ratio$\cdot(\psi-\psi_2)+\cos\alpha_1$, slope ratio= $(\cos\alpha_2 - \cos\alpha_1)/(\psi_1-\psi_2)$, and R_L is the curvature of leg as shown in Fig 3.

B. Aerodynamic Drag

Aerodynamic drag acts on the wings and body of the vehicle as it moves above the water surface. As seen in [6], we can model the aerodynamic drag $F_{D,body}$ for interfacial fliers as follows:

$$F_{D,body} = \frac{1}{2}\rho_{air} C_{D,body} \pi b_1 b_2 v_x^2, \tag{4}$$

where ρ_{air} is the density of air, $C_{D,body}$ is the coefficient of drag, b_1 and b_2 are the major and minor axes of the ellipse from the aft position of the robot, and v_x is the instantaneous speed along the x-axis. For our robot, we use $C_{D,body} = 1.5$, which is the typical coefficient of drag on the body in air for similar-sized interfacial fliers in a low Reynolds number regime, $Re \approx O(10-100)$ [1], [31]. We quantify the Reynolds number $Re = UD/\nu_{air}$, U is the instantaneous speed of the robot (estimated to be between $0.01\,\mathrm{m\,s^{-1}}$ to $1.3\,\mathrm{m\,s^{-1}}$ [1], [6], [32]), D is the characteristic length of the legs (aluminimum wire diameter, 0.33mm), and ν_a is the kinematic viscosity of air. Furthermore, we define $b_1 = 28\times10^{-3}$ m and $b_2 = 8\times10^{-3}$ m.

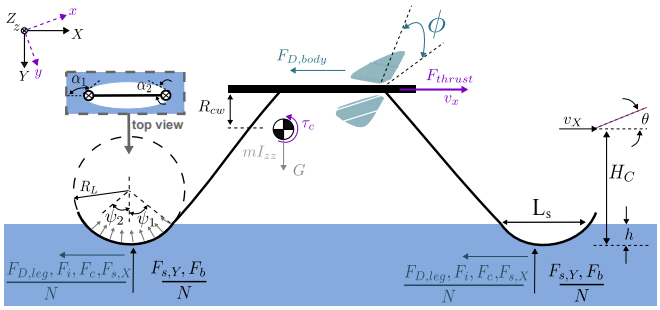

Fig. 3. 2D schematic representation of the dynamics for flapping wing interfacial locomotion

C. Water Drag

On the water's surface, the robot has a Reynolds number of approximately 30-160 (substituting the kinematic viscosity of air for water). In this regime, we consider the quasi-steady state water drag at low Reynolds number:

$$F_{D,leg} = N \cdot \frac{1}{2}\rho_w C_{D,leg} D L_s v_x^2, \tag{5}$$

where N is the number of legs and $C_{D,leg}$ is water drag coefficient. The value of the drag coefficient, $C_{D,leg}$, can vary depending on several factors such as the fluid material, the shape of the object, the flow regime (laminar or turbulent), and other physical conditions. To determine the drag coefficient, we modeled our rounded legs as a yawed, finite aspect ratio cylinder with an angle of inclination of 23°, based on the shape of our legs. From previous results [33], cylinders with large aspect ratios ($L/D = 20$) in a low Reynolds number regime (Re < 40) have a resulting drag coefficient, $C_{D,leg} = 1.55$.

D. Additional Forces

As the robot generates momentum on the water's surface, the resulting capillary wave produces a drag force on the robot [30]. As the robot leg $R \ll H \ll l_c$ and the speed exceeds and closes the capillary wave velocity threshold (c_{min} =$0.23\,\mathrm{m\,s^{-1}}$), the capillary wave drag increases with increasing leg speed, according to the dipolar approximation [24]:

$$F_c \simeq N \cdot \rho_w c_{min}^2 l_c \sqrt{\frac{v_x}{c_{min}} - 1} \cdot D \cdot H(v_x - c_{min}), \tag{6}$$

where $c_{min} = (4g\gamma/\rho_w)^{1/4}$ [24], and $H()$ is the Heaviside function.

We can also consider the force of the added mass of the water as the robot accelerates: $F_i = m_i a_i$, where the added mass is defined as, $m_i = \pi\rho_w (D/2)^2 (N \cdot L_s)$.

Given these representations, we can see that the water drag has a significantly larger effect than the air drag on the body $F_{D,body}/F_{D,leg} \sim 5\times10^{-2}$, the force contributed by the added mass of the water $F_i/F_{D,leg} \sim 5\times10^{-3}$, the capillary force $F_c/F_{D,leg} \sim 5\times10^{-2}$, and the surface tension in the horizontal direction $F_{s,X}/F_{D,leg} \sim 5\times10^{-2}$.

IV. Model Validation

We ran a number of experiments to validate the force relationships presented in the previous section. In the horizontal direction, we characterized the velocity of the vehicle in two distinct regimes. First, as the robot is generating thrust, the velocity should asymptotically increase with time. Second, when the robot stops flapping its wings, the robot's velocity should asymptotically decay due to the effect of water drag and capillary forces. In the vertical direction, we quantified the surface tension force in relation to the height of the meniscus, and validated our simple force balance.

A. Thrust Force

In order to validate the force balance in Eq. 1 and characterize the robot's velocity, we need to quantify the thrust force that the robot can generate. Similar to the method described in [34], we perform open-loop flight tests and measure the peak and mean accelerations (α) of the robot during free flight: $F_{thrust} = m(\alpha + g) + F_{D,body}$.

First, we performed static tests on the robot to determine the resonant frequency and operating condition to achieve flapping kinematics similar to those described in [25]. In these tests, the robot is rigidly fixed, and high voltage ($< 200\,\mathrm{V}$), time-varying signals were supplied by a real-time target machine (Speedgoat) and high voltage amplifiers (PZD350A, Trek Amplifiers) through a thin, 52-gauge wire tether to the robot. We recorded the flapping kinematics using high speed video (VEO 710, Phantom). We observed resonant behavior of the flapping wings at an operating condition of $150\,\mathrm{V}$ and $165\,\mathrm{Hz}$, similar to results presented in [25]. The robot (without legs) was then positioned in a flight arena, hung above the ground using kevlar thread at a distance greater than $3\times$ wingspan to avoid ground reaction forces [35]. Both the kevlar thread and wire tether impart minimal torques on the robot in free flight [36].

High speed video captured at 7500 fps recorded the position of the robot during flight. We used the vision.PointTracker toolbox in MATLAB, defining the boundary tracking box of the robot in the frame and collecting the displacement data of the centroids. A third-order polynomial Savitzky-Golay smoothing filter eliminated tracking noise and a low-pass Butterworth filter at $25\,\mathrm{Hz}$ (the first peak of the raw velocity data) derived the mean acceleration. The vehicle has a maximum thrust force of $139\,\mathrm{mg}$, with a mean thrust force of $134\,\mathrm{mg}$.

B. Open-loop Operation on the Water Surface

In order to characterize the dynamic behavior of the γ-bot, we needed to record the position of the robot during interfacial flight tests. We built a clear acrylic tank $29\,\mathrm{cm}$ in length, corresponding to 5 body lengths of the robot. At the start of the experiment, we positioned the robot at one end of the tank and ensured the wire tether had sufficient slack to prevent the addition of external forces and torques. Using the experimental setup described above, we tracked the position of the robot during short $t =\sim 1$ s experiments, where the robot flaps its wings for $t = 0.4 - 0.5$ s, increasing in velocity until reaching a steady state, and then stops flapping to glide with decreasing speed. We quantified the velocity and displacement of the robot for two maximum velocity conditions to verify the accuracy of our model. To vary velocity while keeping thrust force constant, we added small weights to the vehicle to increase the depth of the meniscus, increasing the drag forces on the robot and lowering the maximum velocity. Figure 4a shows the results for a $208\,\mathrm{mg}$ robot, while Fig. 4b shows the results for a $304\,\mathrm{mg}$ robot. For each operating condition, we drove the robot a total of three times with the same drive signal, and Fig. 4a,b plot the mean and standard deviation of velocity with respect to time.

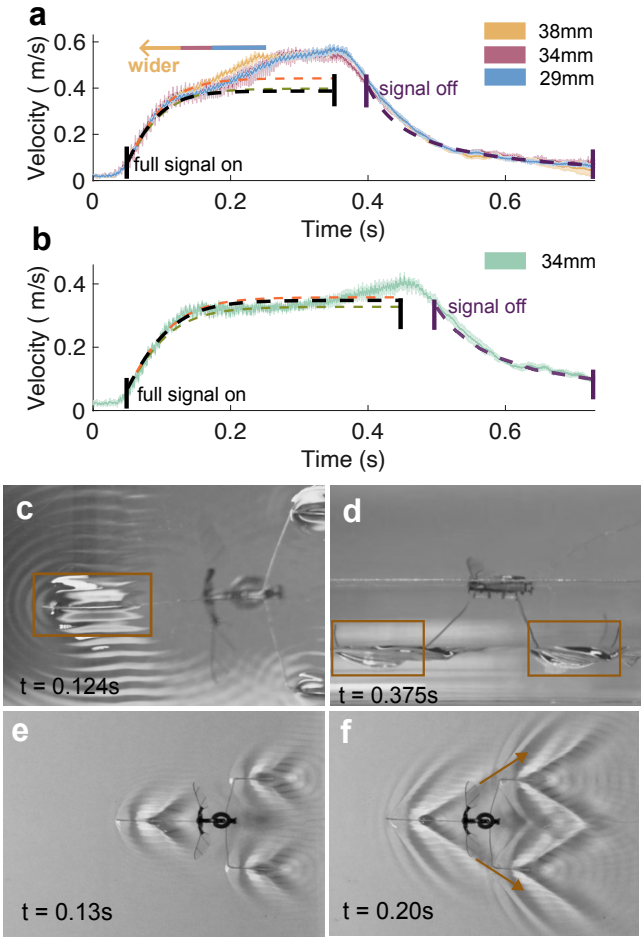

Fig. 4. Horizontal velocity characterization. a) Robot is driven with a constant signal of 150V and 165Hz, weighing 208 mg. The predicted velocity during the drive phase "full signal on" and the passive phase "signal off" are shown in dashed lines with different models (as described in Sect. IV-B). Experimental results (mean and standard deviation) are shown in the yellow, red, and blue traces (colors correspond to leg spacing; see legend). b) Repeated experiment to a) with the robot weighing 304 mg. c,d) Bottom view and side view of the flight experiment. Robot weighs 304 mg. As the skates, ripples are generated by the legs with measured contact angles, and the meniscus loses contact with the rear part of each leg. e,f) Stills from a flight experiment. Robot weighs 208 mg and has a leg spacing of 38 mm. As the robot generates thrust, the wave tunnel generated by the front leg intersects the meniscus of the back leg (brown arrows).

To increase the lifetime of the piezoelectric actuators, we prescribe a short period at the start and end of the experiments for the drive signal to ramp to the desired

voltage [37]. During these periods, the robot is able to generate some velocity, but because we do not have accurate thrust force measurements at these conditions, we neglect these time periods in our model predictions and only consider instances when the wings are flapping at either maximum drive amplitude (150 V) or the minimum amplitude (0 V).

The plots show good prediction of robot behavior while the robot is actively moving across the water's surface and when it is gliding. While the robot is flapping its wings, we predict an asymptotic increase in velocity, see Fig. 4a,b dashed lines. The green dashed line represents the full dynamic model of Eq. 1. We experimentally measured the contact angles (α_1 and α_2) in Eq. 3 as well as the wetted length (L_s) in Eq. 5 using high speed videography, shown in Fig. 4c,d. The wetted length shortens during operation due to the meniscus separating from the leg. Based on the previous section, water drag has a larger effect on performance compared to surface tension and capillary force by at least two orders of magnitude. A simplified model, without the effects of $F_{s,X}$ and F_c, is shown in the orange dashed line, which slightly overestimates the measured velocity profile due to the shortened wetted length. The black dashed line represents a further simplification, using the predicted wetted length of the leg instead of experimentally measured value, eliminating the need to measure the shortened meniscus. In the glide phase, Eq. 1 we can eliminate the effects of air drag on the wings, isolating the drag contributions imparted by the water interface. We plotted the predicted velocity profile (purple dashed line), which aligns with the experimentally collected data.

For the lighter vehicle in Fig. 4a, we observe a second increase in velocity, which we predict is due to the back legs moving through a low pressure tunnel created by the front leg, see Fig. 4e,f. Similar effects can be observed in schools of fish [38]. To elucidate this effect, we modified the positions of the back legs, varying the distance between the legs from 29 mm to 38 mm. As can be seen in Fig. 4a, as the legs increase in width closer to the position of the low pressure tunnel, the robot's velocity begins to increase earlier, and deviates more sharply from the predicted steady state condition. Future work intends to model this effect in more detail.

C. Payload capacity

Equation 2 relates the height of the meniscus with the resultant force from surface tension. We can therefore quantify the total payload that the robot is able to carry before breaking the meniscus. Increased payload capacity will allow for future untethered operation, providing additional support for sensors, drive electronics, and control systems. The model prediction is plotted in Fig. 5a (purple). As can be seen in Fig. 5b, we utilized a $30.2\,\mathrm{cm}$ carbon fiber rod to amplify the measured torque of a 6-axis force sensor (Nano17 Titanium, ATI) to measure the total payload capacity. After static calibration, we attached the carbon fiber rod to the robot's center of mass, ensuring that the vertical surface tension was evenly distributed across the robot's legs. We obtained the

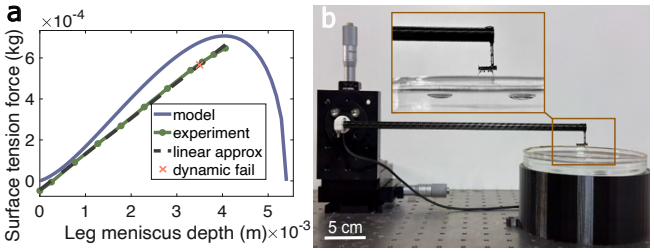

Fig. 5. Surface tension force with respect to leg meniscus depth. a) Model results (purple solid line) and experiment data (green solid line). The maximum static weight supported by the meniscus = 647 mg, the maximum weight for the dynamic case was 566 mg. b) Experimental setup.

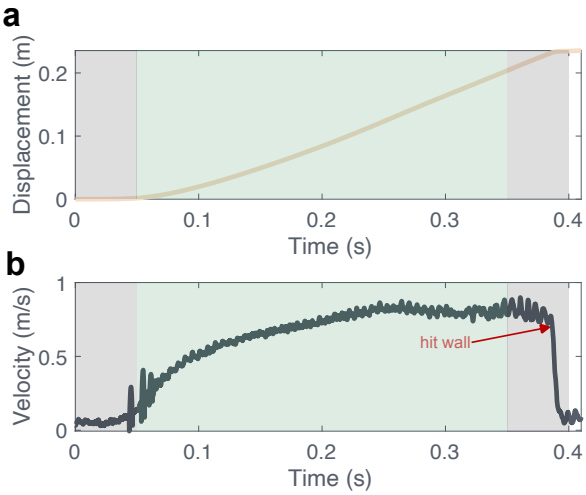

Fig. 6. Peak velocity of robot. a) The robot's linear displacement on the water surface. b) The linear velocity on the water interface.

height of the meniscus by adjusting the XYZ stage (PT3, Thorlabs). The experimental results are plotted in green in Fig. 5a. The maximum vehicle weight that the current design can support is $647\,\mathrm{mg}$ total mass, slightly less than the predicted maximum of $707\,\mathrm{mg}$. This discrepancy was also seen in [17], as the real contact length decreases with the deformation of the water surface, decreasing the actual surface tension acting on the robot.

V. Robot Demonstrations

In addition to validating the physical model, we wanted to demonstrate robot performance in terms of maximum speed, turning angle, and payload while flapping. Payload during dynamic operation is a critical metric, as the wings and body oscillations will generate ripples on the water's surface effecting the height of the meniscus.

A. Robot Velocity

To quantify the maximum robot velocity, we drove γ-bot at the resonant frequency with zero additional payload, minimizing the height of the meniscus and thus decreasing water drag. As can be seen in Fig. 6, γ-bot reaches steady state velocity of $0.9\,\mathrm{m\,s^{-1}}$ around $t = 0.2$ s. Before the end of the experiment, γ-bot reached the restraining wall at the end of the tank and sharply decreased in velocity during the ramp down period.

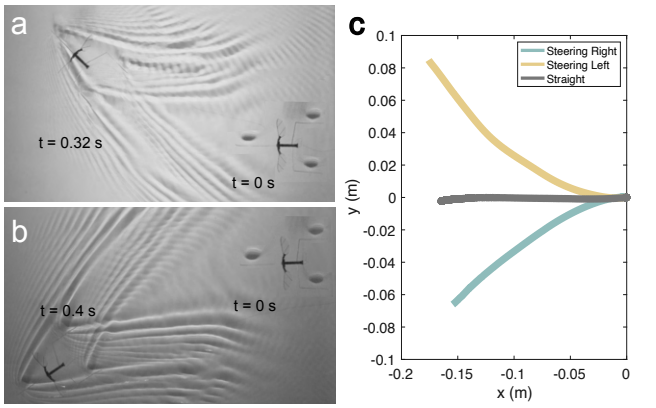

Fig. 7. Steering experiment. a) Right turn, left and right actuators driven at 150V and 100V, respectively, at 165Hz. b) Left turn, left, and right actuators driven at 80V and 150V, respectively, at 165Hz. c) Trajectories of steering experiments, straight (gray), right turn (yellow), left turn (green).

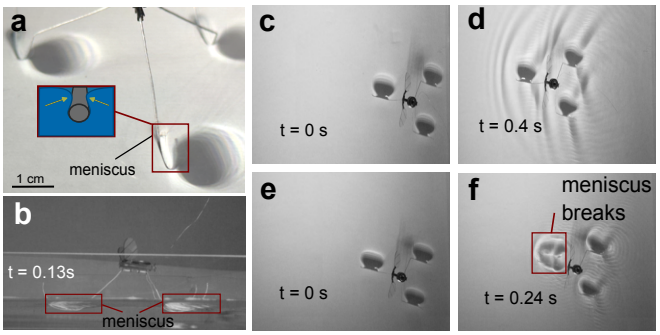

Fig. 8. Meniscus with critical body weight. a) Top view of the meniscus with a 566 mg robot, diagram of the meniscus edges on top of the leg (inset). b) The side view of meniscus during operation. c,d) Still shots (top view) of a successful interfacial flight at 531 mg as total mass. e,f) Still shots (top view) of an unsuccessful interfacial flight at 566 mg as total mass, the meniscus breaks at the start of the test.

In addition to quantifying maximum velocity, we ran the γ-bot under various operating conditions, lowering the drive voltage from 150V to 60V. At 60V, the robot can still generate momentum and travel across the water surface at $1.5\,\mathrm{BL/s}$. For future autonomous operation, lowering the drive voltage is an essential aspect to increase the efficiency of the power electronics.

B. Steering

By providing asymmetric forces to the wings, we can generate a net torque around the robot's center of mass to initiate turns. Steering increases the workspace of the robot, allowing it to locomote to any destination in the 2D plane. We generated asymmetric forces by commanding drive signals of different amplitudes to the left and right wings. Driving the left wing at 150V and the right wing at 100V created a larger thrust force on the left side of the center of mass, resulting in a right turn in approximately $0.32\,\mathrm{s}$, as seen in Fig. 7a. By driving the left wing at 80V and the right wing at 150V, we can initiate a left turn in $0.4\,\mathrm{s}$, as seen in Fig. 7b. The discrepancy in drive voltage is due to slight variations between the robot halves during assembly. While not modeled in Sect. III, we can demonstrate that the robot is able to overcome additional drag forces along the horizontal length of the leg (not just the cross-sectional diameter). Trajectories in the 2D plane can be seen in Fig. 7c.

C. Payload during Interfacial Flight

When the robot flaps its wings, the thrust force periodically moves from below the vehicle to above the vehicle as the wings move through the full flapping amplitude. This results in periodic waves on the water surface as the robot's body oscillates, disturbing the meniscus, and increasing the likelihood that the distal tip breaks the air-water interface. This is exacerbated by the narrowing of the meniscus at high payloads, as seen in Fig. 8a. Additionally, Fig. 8b demonstrates that the meniscus on the back legs is smaller than on the front, minimizing the expected amount of surface tension force. In our experiments (represented in Fig. 8c-f), we observed that the robot can carry a total weight of $419\,\mathrm{mg}$ without breaking the water surface. At $454\,\mathrm{mg}$ payload, the meniscus ruptures and the legs enter the water.

VI. Conclusion and Future Work

We developed a novel robotic platform, the γ-bot, a 112 mg robot that exploits surface tension to remain on the water surface and generate thrust force with flapping wings, a locomotion strategy known as interfacial flight. By orienting the thrust vector parallel to the water's surface, we can generate large steady-state velocities up to $0.9\,\mathrm{m\,s^{-1}}$. By independently driving the wings, we can initiate turns, increasing the workspace of the vehicle for future operations. The design of the legs resulted in a surface tension force that supports an additional $419\,\mathrm{mg}$ onboard the vehicle for future autonomy experiments. We presented a simple one-dimensional model for horizontal velocity, and validated our assumptions across multiple operating conditions.

In future, we will integrate mm-scale drive electronics to autonomously power the vehicle [34], [39]. We will explore the vehicle's design space (e.g., shape and length of leg, wing size, flapping frequency, and flapping amplitude) to decrease cost of transport and increase the efficiency of power electronics. Because the robot passively rests on the water surface, we can explore intermittent flight strategies to conserve power, where periods of passive gliding are interspersed with active periods of interfacial flight. In an effort to move this platform out of the laboratory environment, we will also characterize mm-scale sensing and control strategies to integrate onto a lightweight embedded system.

Acknowledgment

This work was sponsored in part by the Office of Naval Research (N00014-24-1-2141-P00001). Any opinions, findings, and conclusions or recommendations expressed in this material are those of the author(s) and do not necessarily reflect the views of the Office of Naval Research.

REFERENCES

[1] J. W. Bush and D. L. Hu, "WALKING ON WATER: Biolocomotion at the Interface," *Annual Review of Fluid Mechanics*, vol. 38, no. 1, pp. 339–369, Jan. 2006. [Online]. Available: https://www.annualreviews.org/doi/10.1146/annurev.fluid.38.050304.092157

[2] J. W. Bush, D. L. Hu, and M. Prakash, "The Integument of Water-walking Arthropods: Form and Function," in *Advances in Insect Physiology*. Elsevier, 2007, vol. 34, pp. 117–192. [Online]. Available: https://linkinghub.elsevier.com/retrieve/pii/S0065280607340034

[3] X. Gao and L. Jiang, "Water-repellent legs of water striders," *Nature*, vol. 432, no. 7013, pp. 36–36, Nov. 2004. [Online]. Available: https://www.nature.com/articles/432036a

[4] C. Ellington, "The novel aerodynamics of insect flight: applications to micro-air vehicles," *Journal of Experimental Biology*, vol. 202, no. 23, pp. 3439–3448, Dec. 1999. [Online]. Available: https://doi.org/10.1242/jeb.202.23.3439

[5] C. Roh and M. Gharib, "Honeybees use their wings for water surface locomotion," *Proceedings of the National Academy of Sciences*, vol. 116, no. 49, pp. 24 446–24 451, Dec. 2019. [Online]. Available: https://pnas.org/doi/full/10.1073/pnas.1908857116

[6] H. Mukundarajan, T. C. Bardon, D. H. Kim, and M. Prakash, "Surface tension dominates insect flight on fluid interfaces," *Journal of Experimental Biology*, vol. 219, no. 5, pp. 752–766, Mar. 2016. [Online]. Available: https://journals.biologists.com/jeb/article/219/5/752/16640/Surface-tension-dominates-insect-flight-on-fluid

[7] D. L. Hu, B. Chan, and J. W. M. Bush, "The hydrodynamics of water strider locomotion," *Nature*, vol. 424, no. 6949, pp. 663–666, Aug. 2003. [Online]. Available: https://www.nature.com/articles/nature01793

[8] Y. S. Song and M. Sitti, "STRIDE: A Highly Maneuverable and Non-Tethered Water Strider Robot," in *Proceedings 2007 IEEE International Conference on Robotics and Automation*. Rome, Italy: IEEE, Apr. 2007, pp. 980–984, iSSN: 1050-4729. [Online]. Available: http://ieeexplore.ieee.org/document/4209216/

[9] S. H. Suhr, Y. Seong Song, S. Jun Lee, and M. Sitti, "Biologically Inspired Miniature Water Strider Robot," in *Robotics: Science and Systems I*. Robotics: Science and Systems Foundation, Jun. 2005. [Online]. Available: http://www.roboticsproceedings.org/rss01/p42.pdf

[10] H. Takonobu, K. Kodaira, and H. Takeda, "Water strider's muscle arrangement-based robot," in *2005 IEEE/RSJ International Conference on Intelligent Robots and Systems*. Edmonton, Alta., Canada: IEEE, 2005, pp. 1754–1759. [Online]. Available: http://ieeexplore.ieee.org/document/1545355/

[11] O. Ozcan, H. Wang, J. D. Taylor, and M. Sitti, "STRIDE II: A Water Strider-inspired Miniature Robot with Circular Footpads," *International Journal of Advanced Robotic Systems*, vol. 11, no. 6, p. 85, Jun. 2014, publisher: SAGE Publications. [Online]. Available: https://doi.org/10.5772/58701

[12] J. Yan, K. Yang, G. Liu, and J. Zhao, "Flexible Driving Mechanism Inspired Water Strider Robot Walking on Water Surface," *IEEE Access*, vol. 8, pp. 89 643–89 654, 2020.

[13] J. Zhao, X. Zhang, N. Chen, and Q. Pan, "Why Superhydrophobicity Is Crucial for a Water-Jumping Microrobot? Experimental and Theoretical Investigations," *ACS Applied Materials & Interfaces*, vol. 4, no. 7, pp. 3706–3711, Jul. 2012. [Online]. Available: https://pubs.acs.org/doi/10.1021/am300794z

[14] X. Zhang, J. Zhao, Q. Zhu, N. Chen, M. Zhang, and Q. Pan, "Bioinspired Aquatic Microrobot Capable of Walking on Water Surface Like a Water Strider," *ACS Applied Materials & Interfaces*, vol. 3, no. 7, pp. 2630–2636, Jul. 2011. [Online]. Available: https://pubs.acs.org/doi/10.1021/am200382g

[15] K. Suzuki, H. Takanobu, K. Noya, H. Koike, and H. Miura, "Water strider robots with microfabricated hydrophobic legs," in *2007 IEEE/RSJ International Conference on Intelligent Robots and Systems*. San Diego, CA, USA: IEEE, Oct. 2007, pp. 590–595. [Online]. Available: http://ieeexplore.ieee.org/document/4399460/

[16] D. Kim, M. Gwon, B. Kim, V. M. Ortega-Jimenez, S. Han, D. Kang, M. S. Bhamla, and J.-S. Koh, "Design of a Biologically Inspired Water-Walking Robot Powered by Artificial Muscle," *Micromachines*, vol. 13, no. 4, 2022.

[17] J.-S. Koh, E. Yang, G.-P. Jung, S.-P. Jung, J. H. Son, S.-I. Lee, P. G. Jablonski, R. J. Wood, H.-Y. Kim, and K.-J. Cho, "Jumping on water: Surface tension–dominated jumping of water striders and robotic insects," *Science*, vol. 349, no. 6247, pp. 517–521, Jul. 2015. [Online]. Available: https://www.science.org/doi/10.1126/science.aab1637

[18] D. L. Hu, M. Prakash, B. Chan, and J. W. M. Bush, "Water-walking devices," *Experiments in Fluids*, vol. 43, no. 5, pp. 769–778, Nov. 2007. [Online]. Available: http://link.springer.com/10.1007/s00348-007-0339-6

[19] B. Kwak, D. Lee, and J. Bae, "Flexural Joints for Improved Linear Motion of a Marangoni Propulsion Robot: Design and Experiment," in *2018 7th IEEE International Conference on Biomedical Robotics and Biomechatronics (Biorob)*. Enschede: IEEE, Aug. 2018, pp. 1321–1326. [Online]. Available: https://ieeexplore.ieee.org/document/8488118/

[20] M. L. Timm, S. Jafari Kang, J. P. Rothstein, and H. Masoud, "A remotely controlled Marangoni surfer," *Bioinspiration & Biomimetics*, vol. 16, no. 6, p. 066014, Nov. 2021. [Online]. Available: https://iopscience.iop.org/article/10.1088/1748-3190/ac253c

[21] B. Kwak, S. Choi, J. Maeng, and J. Bae, "Marangoni effect inspired robotic self-propulsion over a water surface using a flow-imbibition-powered microfluidic pump," *Scientific Reports*, vol. 11, no. 1, p. 17469, Sep. 2021. [Online]. Available: https://www.nature.com/articles/s41598-021-96553-8

[22] S. Zhou, W. Zhang, Y. Zou, X. Ke, F. Cui, and W. Liu, "Piezoelectric driven insect-inspired robot with flapping wings capable of skating on the water," *Electronics Letters*, vol. 53, no. 9, pp. 579–580, Apr. 2017. [Online]. Available: https://onlinelibrary.wiley.com/doi/10.1049/el.2017.0186

[23] Y. M. Chukewad, J. James, A. Singh, and S. Fuller, "RoboFly: An Insect-Sized Robot With Simplified Fabrication That Is Capable of Flight, Ground, and Water Surface Locomotion," *IEEE Transactions on Robotics*, vol. 37, no. 6, pp. 2025–2040, Dec. 2021.

[24] A. D. Chepelianskii, M. Schindler, F. Chevy, and E. Raphaël, "Self-consistent theory of capillary-gravity-wave generation by small moving objects," *Physical Review E*, vol. 81, no. 1, p. 016306, Jan. 2010. [Online]. Available: https://link.aps.org/doi/10.1103/PhysRevE.81.016306

[25] N. T. Jafferis, M. A. Graule, and R. J. Wood, "Non-linear resonance modeling and system design improvements for underactuated flapping-wing vehicles," in *2016 IEEE International Conference on Robotics and Automation (ICRA)*. Stockholm, Sweden: IEEE, May 2016, pp. 3234–3241. [Online]. Available: http://ieeexplore.ieee.org/document/7487493/

[26] R. J. Wood, S. Avadhanula, R. Sahai, E. Steltz, and R. S. Fearing, "Microrobot Design Using Fiber Reinforced Composites," *Journal of Mechanical Design*, vol. 130, no. 5, p. 052304, May 2008. [Online]. Available: https://asmedigitalcollection.asme.org/mechanicaldesign/article/doi/10.1115/1.2885509/458340/Microrobot-Design-Using-Fiber-Reinforced

[27] W. Carden, L. Geng, D. Matlock, and R. Wagoner, "Measurement of springback," *International Journal of Mechanical Sciences*, vol. 44, no. 1, pp. 79–101, Jan. 2002. [Online]. Available: https://www.sciencedirect.com/science/article/pii/S0020740301000820

[28] J. B. Keller, "Surface tension force on a partly submerged body," *Physics of Fluids*, vol. 10, no. 11, pp. 3009–3010, Nov. 1998. [Online]. Available: https://doi.org/10.1063/1.869820

[29] D. Vella and J. Li, "The impulsive motion of a small cylinder at an interface," *Physics of Fluids*, vol. 22, no. 5, p. 052104, May 2010. [Online]. Available: https://doi.org/10.1063/1.3427241

[30] E. Raphaël and P.-G. De Gennes, "Capillary gravity waves caused by a moving disturbance: Wave resistance," *Physical Review E*, vol. 53, no. 4, pp. 3448–3455, Apr. 1996. [Online]. Available: https://link.aps.org/doi/10.1103/PhysRevE.53.3448

[31] W. Nachtigall, "Aerodynamic coefficients for hymenopteran bodies," *Naturwissenschaften*, vol. 78, no. 12, pp. 567–569, Dec. 1991. [Online]. Available: http://link.springer.com/10.1007/BF01134452

[32] B. Kwak and J. Bae, "Locomotion of arthropods in aquatic environment and their applications in robotics," *Bioinspiration & Biomimetics*, vol. 13, no. 4, p. 041002, May 2018. [Online]. Available: https://iopscience.iop.org/article/10.1088/1748-3190/aab460

[33] A. Vakil and S. I. Green, "Corrigendum to "Drag and lift coefficients of inclined finite circular cylinders at moderate Reynolds numbers" [Computers & Fluids 38 (2009) 1771–1781]," *Computers & Fluids*, vol. 74, p. 126, Mar. 2013. [Online]. Available: https://www.sciencedirect.com/science/article/pii/S0045793013000662

[34] N. T. Jafferis, E. F. Helbling, M. Karpelson, and R. J. Wood, "Untethered flight of an insect-sized flapping-wing microscale aerial vehicle," *Nature*, vol. 570, no. 7762, pp. 491–495, Jun. 2019. [Online]. Available: http://www.nature.com/articles/s41586-019-1322-0

[35] Jeremy M. V. Rayner, "On the Aerodynamics of Animal Flight in Ground Effect," *Philosophical Transactions: Biological Sciences*, vol. 334, no. 1269, pp. 119–128, 1991, publisher: The Royal Society. [Online]. Available: http://www.jstor.org/stable/55562

[36] K. Y. Ma, P. Chirarattananon, S. B. Fuller, and R. J. Wood, "Controlled Flight of a Biologically Inspired, Insect-Scale Robot," *Science*, vol. 340, no. 6132, pp. 603–607, May 2013. [Online]. Available: https://www.science.org/doi/10.1126/science.1231806

[37] N. T. Jafferis, M. J. Smith, and R. J. Wood, "Design and manufacturing rules for maximizing the performance of polycrystalline piezoelectric bending actuators," *Smart Materials and Structures*, vol. 24, no. 6, p. 065023, Jun. 2015. [Online]. Available: https://iopscience.iop.org/article/10.1088/0964-1726/24/6/065023

[38] C. K. Hemelrijk and H. Hildenbrandt, "Schools of fish and flocks of birds: their shape and internal structure by self-organization," *Interface focus*, vol. 2, no. 6, pp. 726–737, 2012, publisher: The Royal Society.

[39] J. James, V. Iyer, Y. Chukewad, S. Gollakota, and S. B. Fuller, "Liftoff of a 190 mg Laser-Powered Aerial Vehicle: The Lightest Wireless Robot to Fly," in *2018 IEEE International Conference on Robotics and Automation (ICRA)*, May 2018, pp. 3587–3594, journal Abbreviation: 2018 IEEE International Conference on Robotics and Automation (ICRA).